THE JOURNAL OF PHYSICAL CHEMISTRY Letters

Letter

Cite This: J. Phys. Chem. Lett. 2018, 9, 1739−1745

pubs.acs.org/JPCL

Correlating Li^+-Solvation Structure and its Electrochemical Reaction Kinetics with Sulfur in Subnano Confinement

Chengyin Fu,[†,⊥] Lihua Xu,[†,⊥] Fredy W. Aquino,[‡] Arthur v. Cresce,[§] Mallory Gobet,[∥] Steven G. Greenbaum,[∥] Kang Xu,[§] Bryan M. Wong,*[,†,‡] and Juchen Guo*[,†,‡]

[†]Department of Chemical and Environmental Engineering, University of California-Riverside, Riverside, California 92521, United States

[‡]Materials Science and Engineering Program, University of California-Riverside, Riverside, California 92521, United States

[§]U.S. Army Research Laboratory, Adelphi, Maryland 20783, United States

[∥]Department of Physics and Astronomy, Hunter College of the City University of New York, New York, New York 10065, United States

Supporting Information

ABSTRACT: Combining theoretical and experimental approaches, we investigate the solvation properties of Li^+ ions in a series of ether solvents (dimethoxyethane, diglyme, triglyme, tetraglyme, and 15-crown-5) and their subsequent effects on the solid-state lithium−sulfur reactions in subnano confinement. The *ab initio* and classical molecular dynamics (MD) simulations predict Li^+ ion solvation structures within ether solvents in excellent agreement with experimental evidence from electrospray ionization-mass spectroscopy. An excellent correlation is also established between the Li^+-solvation binding energies from the *ab initio* MD simulations and the lithiation overpotentials obtained from galvanostatic intermittent titration techniques (GITT). These findings convincingly indicate that a stronger solvation binding energy imposes a higher lithiation overpotential of sulfur in subnano confinement. The mechanistic understanding achieved at the electronic and atomistic level of how Li^+-solvation dictates its electrochemical reactions with sulfur in subnano confinement provides invaluable guidance in designing future electrolytes and electrodes for Li-sulfur chemistry.

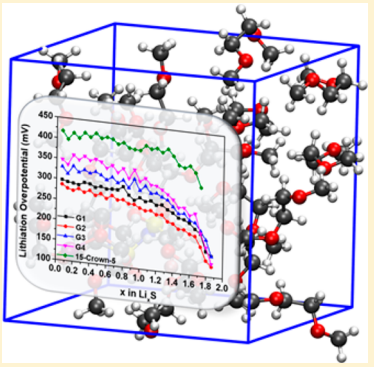

An intrinsic materials challenge in lithium−sulfur (Li−S) batteries using sulfur−carbon composite cathodes and ethereal electrolytes is the dissolution of intermediate lithium polysulfides during lithiation and delithiation reactions of sulfur. The presence of polysulfides in the electrolyte leads to numerous problems including the loss of active species, redistribution of sulfur in the cathode, passivation/consumption of the lithium anode, and the notorious shuttling effect during delithiation.[1−4] On the other hand, it is also essential to have lithium polysulfides in the solution in order for the sulfur to be fully utilized, which would be otherwise impossible due to the insulating nature of elemental sulfur. Therefore, the dissolution of lithium polysulfides presents a fundamental dilemma in the design of Li−S batteries, and new paradigms of Li−S electrochemical reactions need to be explored. In a previous study, we proposed a solid-state Li−S reaction mechanism enabled by subnano confinement of sulfur.[5] When sulfur is confined in carbon pores smaller than 1 nm, the accessibility of the electrolyte is limited by the size of the sulfur-confining pore. As a result, Li−S electrochemical reactions in these subnano pores occur in the solid or quasi-solid state, which are characterized by a distinct electrochemical behavior that differs from conventional solution-phase Li−S reactions.[6−10] The solid-state Li−S mechanism was also reported by Wang et al.[11] and Li et al.[12] Aurbach and co-workers also proposed a similar mechanism emphasizing the formation of a solid electrolyte interphase (SEI) sealing the subnano pores to prevent electrolyte penetration.[13,14] A great advantage of this solid-state Li−S electrochemical mechanism is the compatibility with different types of electrolytes, including carbonate-based electrolytes, which would not work with conventional sulfur cathodes. Our previous study demonstrated a higher overpotential for sulfur lithiation in tetraglyme (G4) compared to ethylene carbonate/diethyl carbonate,[5] which clearly indicates that the properties of solvated Li^+ could affect the proposed solid-state Li−S reaction mechanism. Previous studies on solvation properties of organic Li^+ electrolytes also indicated profound effects of Li^+ ion solvation on electrochemical reactions.[15−18]

In this study, we systematically investigate these solvation effects in a series of electrolytes based on ether solvents including dimethoxyethane (G1), diglyme (G2), triglyme (G3), G4, and 1,4,7,10,13-pentaoxacyclopentadecane (15-crown-5). Our selection encompasses ether molecules with a clear

Received: February 21, 2018
Accepted: March 17, 2018
Published: March 17, 2018

DOI: 10.1021/acs.jpclett.8b00567
J. Phys. Chem. Lett. 2018, 9, 1739−1745

systematic structure variation, which provides a rigorous comparison of their solvation effects. The subnano confined sulfur is prepared via infusion of elemental sulfur into microporous carbon with a pore size exclusively smaller than 1 nm (average pore size 0.67 nm) as described in the Supporting Information. 0.5 M lithium bis(trifluoromethanesulfonyl)imide (LiTFSI) solutions in the ether solvents are used as the electrolytes in this study. As shown in Table 1, from

Table 1. Properties of 0.5 M LiTFSI Electrolytes in Various Ethers at 25 °C

solvent	G1	G2	G3	G4	15-crown-5
conductivity (S m^{-1})	1.10	0.67	0.38	0.23	0.052
Li^+ ion self-diffusion coefficient (10^{-10} m^2 s^{-1})	8.09	3.62	1.76	1.03	0.147

G1 to 15-crown-5, the room temperature ionic conductivity of the electrolytes decreases with the increasing molecular weight of the solvents. The conductivity of the 15-crown-5 electrolyte is more than 4 times lower than that of the G4 electrolyte despite their similar molecular weight (differing by the mass of 2 hydrogen atoms), which can be attributed to the significantly higher viscosity of 15-crown-5 (21.7 cP at 25 °C)[19] than that of G4 (4.05 cP at 25 °C). The Li^+ ion self-diffusion coefficients were measured by ^7Li NMR spectroscopy[20] and display the same trend as the conductivity.

The solvation structures of Li^+ in these ether solvents are theoretically investigated with *ab initio* molecular dynamics (AIMD) simulations, which are described in detail in the Supporting Information. The characteristic Li−O bond lengths between the solvated Li^+ and ether molecules can be obtained from the radial distribution function (RDF) shown in Figure 1 for each of the ether electrolytes. The primary Li−O coordination peaks, originating from the first neighboring oxygen atoms in ether molecules, are around 2.05 Å in all electrolytes, which reflects the radius of the first solvation shell. It is also clear that the preferred coordination number of the Li^+ within the first solvation shell is 4, which is consistent with previous findings.[21−24] The exception is 15-crown-5, whose rigid ring structure of 5 oxygen atoms forces the Li^+ coordination number to lie between 4 and 5. The insets in Figure 1 display the characteristic primary solvation structures for Li^+ with ether molecules obtained from AIMD simulations.

Electrospray Ionization-Mass Spectroscopy (ESI-MS) was used to validate the predicted Li^+ ion solvation structures in the electrolytes, which reveals the positively charged species in all electrolytes as shown in Figure 2. The spectrum of the G1

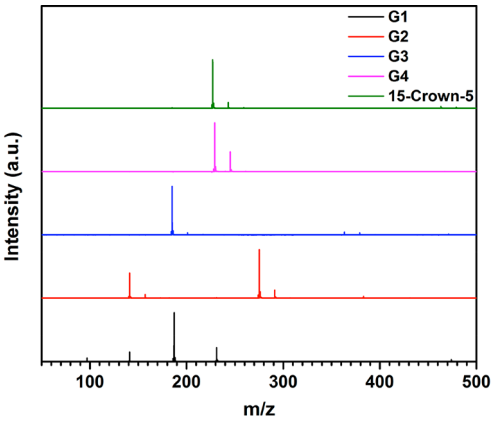

Figure 2. ESI-MS spectra of 0.5 M LiTFSI in G1, G2, G3, G4, and 15-crown-5.

electrolyte shows $[Li(G1)_2]^+$ (m/z = 187.1) as the majority of the solvated Li^+ ions, which suggests that one Li^+ ion coordinated by two G1 molecules constitutes the most stable

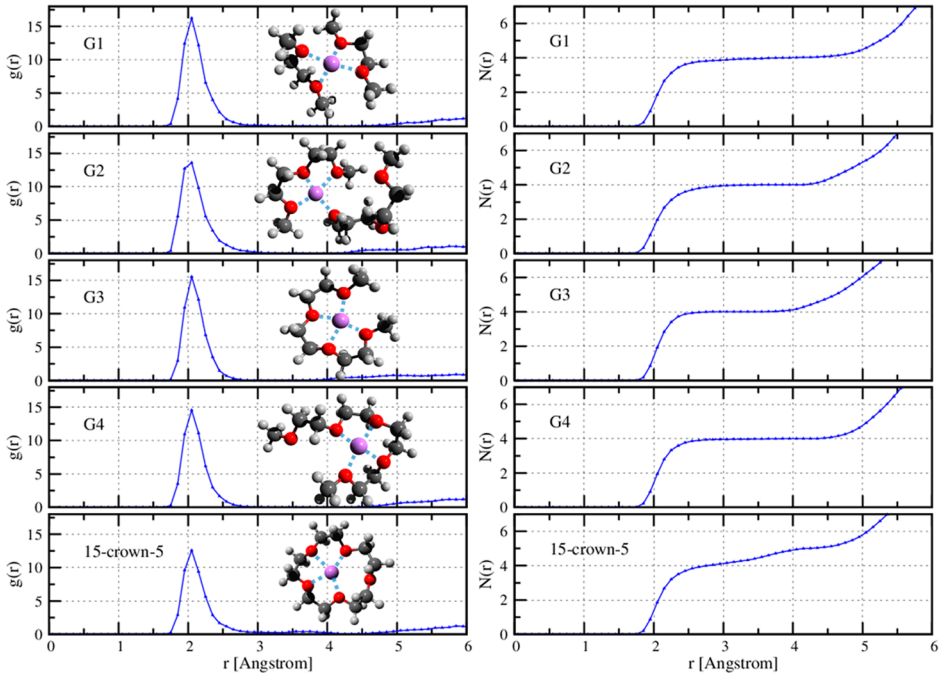

Figure 1. Radial distribution functions, $g(r)$, between Li and O in ether molecules and the corresponding Li^+ coordination number, $N_c(r)$, in a 0.5 M LiTFSI solution in ether. The structures of the first solvation shell of Li^+ ions are shown in the insets. All the plots are obtained from AIMD simulations.

DOI: 10.1021/acs.jpclett.8b00567
J. Phys. Chem. Lett. 2018, 9, 1739−1745

species. It is also very likely the primary solvation shell. Small fractions of $[Li(G1)]^+$ (m/z = 97.1), $[Li(G1)(C_2H_4O)]^+$ (m/z = 141.1), and $[Li(G1)_2(C_2H_4O)]^+$ (m/z= 231.1) also exist in the G1 electrolyte, where the C_2H_4O could be either ethylene oxide (a precursor for G1) or acetaldehyde, the existence of which may be due to partial fragmentation before the solvated species reaches the aperture of the spectrometer.[25] The spectrum of the G2 electrolyte indicates two major solvation species, $[Li(G2)]^+$ (m/z = 141.1) and $[Li(G2)_2]^+$ (m/z = 275.2), and the molar ratio between these two species is approximately 35:65. The spectra of the G3, G4, and 15-crown-5 electrolytes show $[Li(G3)]^+$ (m/z = 185.1), $[Li(G4)]^+$ (m/z = 229.1), and $[Li(15\text{-crown-}5)]^+$ (m/z = 227.1), respectively, as the most abundant signal without rival, suggesting that each Li^+ coordinated by only one ether solvent molecule constitutes the first solvation shell in these three electrolytes.

The ESI-MS spectra results are in striking agreement with the theoretical Li^+ ion solvation structures predicted by AIMD simulations. However, for the case of the G2 electrolyte it was experimentally found that there is a 65% probability that Li^+ coordinates with two G2 molecules as $[Li(G2)_2]^+$, while the rest coordinates with one G2 molecule as $[Li(G2)]^+$. The strong presence of $[Li(G2)_2]^+$ suggests that the number of oxygens provided by a single G2 molecule is insufficient to stabilize Li^+, because the optimum coordination number is 4; hence, a second G2 molecule is required to satisfy this preferred solvation number of 4. On the other hand, this second G2 molecule, with only one of its oxygens interacting with Li^+, is relatively loosely-bound and could not survive during the flight stage of ESI-MS. Such partial desolvation of $[Li(G2)_2]^+$ generates the minority peak of $[Li(G2)]^+$ in ESI-MS. The relative coordination strength between Li^+ and the different G2 molecules should be responsible for the coexistence of $[Li(G2)_2]^+$ and $[Li(G2)]^+$.

It is worth noting that solvation is a dynamic process, which cannot be fully captured by the computationally expensive AIMD simulations due to the short simulation time (15 ps in this study). Therefore, to probe the dynamic solvation process in the G2 electrolyte, we carried out classical MD simulations. Figure 3a illustrates both solvation structures of $[Li(G2)_2]^+$ and $[Li(G2)]^+$. Figure 3b shows the Li−O distances from the three oxygen atoms in one G2 molecule labeled as G2-A in $[Li(G2)_2]^+$ (Figure 3a). The nearly constant Li−O distances within the simulation time (2 ns) indicate a stable coordination between the Li^+ ion and the G2-A molecule. Figure 3c shows the Li−O distance from the fourth oxygen atom in the $[Li(G2)_2]^+$ solvation belonging to either of the two surrounding G2 molecules labeled as G2-B and G2-C in Figure 3a. The Li−O distance from G2-B or G2-C clearly indicates that the fourth Li−O coordination fluctuates with time: (1) around t = 0.2 ns, the O1 atom from G2-B forms a Li−O1 coordination; (2) within the 0.3 to 0.85 ns interval, the O3 atom from G2-C forms a different Li−O3 coordination; and (3) within the 0.95 to 1.8 ns interval, the O1 atom from G2-C forms the Li−O1 coordination again. As a result, the existence of the $[Li(G2)]^+$ solvation structure is clearly observed around t = 0.3, 0.9, 1.2, and 1.9 ns, where the fourth oxygen atom (from either G2-B or G2-C) is not close enough, thus only three oxygen atoms from G2-A remain coordinated with the Li^+ ion.

In addition to the solvation structures, the binding energies of the solvated Li^+ can also be obtained from the AIMD simulations. We hypothesize that the binding energy of the

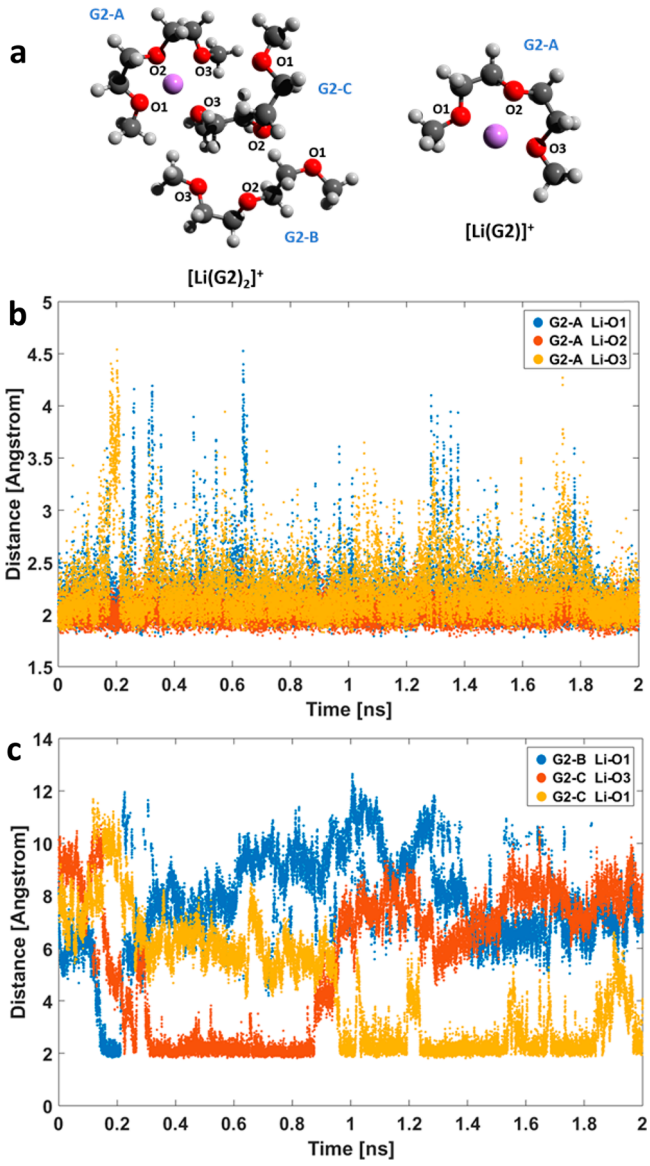

Figure 3. Relative binding strength between Li^+ and two different G2 molecules: (a) $[Li(G2)_2]^+$ and $[Li(G2)]^+$ solvation structures; classical MD simulations of (b) Li−O distance versus time with the oxygen atoms O1, O2, and O3 in the G2-A molecule and (c) Li−O distance versus time from the fourth oxygen in either the G2-B or G2-C molecule.

solvated Li^+ is essential to determine the overpotential of the solid-state Li−S electrochemical reaction in subnano confinement, as a stronger binding energy (higher stability of solvation) would induce a higher energy barrier to desolvate Li^+ for its reaction with sulfur. One theoretical method for assessing the stability of solvated Li^+ at a given temperature is to compute the Gibbs free energy,[26] which is, however, beyond the scope of computationally expensive AIMD simulations due to the requirement of a much larger simulation cell.[26,27] Instead, we investigate the stability of the different solvated systems by calculating the binding energy per Li^+, which is defined by the average difference between the system energy and the sum of all its constituents:[26]

$$E_b = \frac{1}{n}(E_t^{sys} - nE_t^{Li} - nE_t^{TFSI} - n_{eth}E_t^{eth}) \quad (1)$$

DOI: 10.1021/acs.jpclett.8b00567
J. Phys. Chem. Lett. 2018, 9, 1739−1745

where E_b is the binding energy per Li^+ ion, n is the number of LiTFSI pairs (n = 1 in the simulation box), n_{eth} is the total number of ether molecules, and E_t^{sys} is the total energy of the simulation box. Similarly, E_t^{Li}, E_t^{TFSI}, and E_t^{eth} are the total electronic energies of the Li^+ cation, $TFSI^-$ anion, and ether molecule in isolation, respectively. It is important to note that these binding energies include the contribution from the coordinating bonds as well as the ionic bond between the $TFSI^-$ anion and the Li^+ cation. E_b is calculated at each time step during the AIMD simulations as shown in Figure 4, and

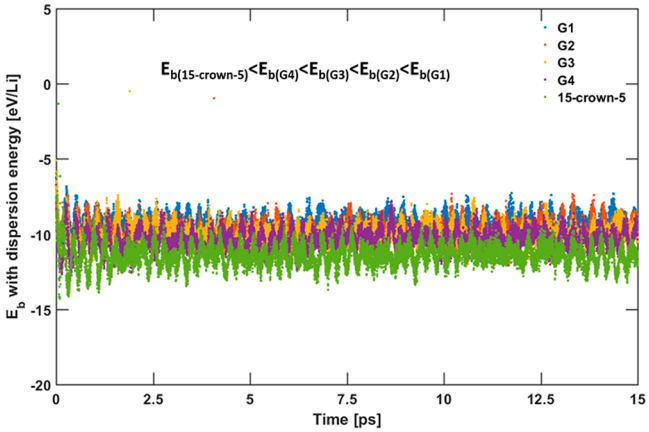

Figure 4. Binding energy of the solvated Li^+ ions in 0.5 M LiTFSI ether electrolytes as a function of AIMD simulation time.

the average E_b is obtained from the last 10 ps of the AIMD simulations as summarized in Table 2. Based on the definition

Table 2. Average Binding Energies of the Solvated Li^+ Ions in 0.5 M LiTFSI Ether Electrolytes Obtained from the Last 10 ps of the AIMD Simulations

system	average E_b (eV)
$[Li(G1)_2]^+$	−9.3833 ± 0.5834
$[Li(G2)_2]^+$	−9.8001 ± 0.6520
$[Li(G3)]^+$	−9.9865 ± 0.6070
$[Li(G4)]^+$	−10.2905 ± 0.6089
$[Li(15\text{-crown-}5)]^+$	−11.4087 ± 0.6371

of the binding energy[26] given in eq 1, the system with the most negative E_b value represents the most stable system. With this convention, we obtain the following numerical order of the binding energies from the most to the least negative (i.e., in order from most to least stable): $E_{b(15\text{-crown-}5)} < E_{b(G4)} < E_{b(G3)} < E_{b(G2)} < E_{b(G1)}$, indicating that the lithiation overpotential of subnano confined sulfur in these electrolytes would display the following order: $\eta_{15\text{-crown-}5} > \eta_{G4} > \eta_{G3} > \eta_{G2} > \eta_{G1}$. It should be pointed out that the solvation binding energy in the G2 electrolyte is calculated based on $[Li(G2)_2]^+$, while both the ESI-MS and classical MD results clearly demonstrate the existence of $[Li(G2)]^+$, which possesses a less stable binding energy than $[Li(G2)_2]^+$, as demonstrated by our density functional theory geometry optimizations shown in the Supporting Information.

The lithiation overpotential of sulfur in subnano confinement can be obtained by galvanostatic intermittent titration techniques (GITT) (experimental details in the Supporting Information). As illustrated in Figure 5a−e, the GITT results in all electrolytes demonstrate an identical quasi-equilibrium lithiation potential profile with a single slope from 2.0 to 1.7 V versus Li/Li^+, indicating a solid solution reaction behavior. Lithiation overpotential is defined by the difference between the quasi-equilibrium potential and the working potential and plotted as a function of Li content as shown in Figure 5f, which displays distinct differences among the electrolytes. The concentration overpotential in these electrolytes under our experimental conditions were determined to be negligible as detailed in the Supporting Information. Therefore, the overpotential in the lithiation of subnano confined sulfur is only attributed to the activation overpotential, which represents the required energy input from equilibrium to enable the lithiation of subnano confined sulfur. The obtained overpotentials clearly indicate the different activation energy barriers for the solid-state Li−S reaction, which can be unambiguously attributed to the different solvation binding energy. Our AIMD simulations suggested activation overpotentials in the following order from the highest to the lowest: $\eta_{15\text{-crown-}5} > \eta_{G4} > \eta_{G3} > \eta_{G2} > \eta_{G1}$, which completely agrees with experiment, with the only exception of G2 (Figure 5f). As previously demonstrated experimentally (ESI-MS) and theoretically (classical MD), the Li^+ solvation in the G2 electrolyte represents a unique case with the coexistence of substantial $[Li(G2)]^+$ species, which should be a less stabilized form than $[Li(G2)_2]^+$ and hence more liable to reacting with sulfur. Therefore, the order of activation overpotentials obtained by GITT, $\eta_{15\text{-crown-}5} > \eta_{G4} > \eta_{G3} > \eta_{G1} > \eta_{G2}$, can be rationalized on the basis of Li^+-solvation structures in the ether electrolytes.

A similar correlation between the Li^+-solvation structure and Li-sulfur reaction kinetics could be obtained from cyclic voltammetry (CV) at various scan rates versus Li^+/Li. As shown in Figure 6a−e, all CV scans display a single pair of redox peaks consistent with the behavior expected from a solid-state Li−S reaction.[5−14] At the lowest scan rate of 0.01 mV s^{-1}, the cathodic (lithiation) peak and anodic (delithiation) peak in all electrolytes are positioned at approximately 1.45 and 2.15 V, respectively. The 0.7 V peak separation indicates the quasi-reversible character of the solid-state lithiation-delithiation of sulfur in subnano confinement. The peak separation increases with increased scan rate, which is also anticipated with the characteristics of quasi-reversible electrochemical reactions. Under a slow scan rate, the electrochemical reaction on the electrode (i.e., the solid-state Li−S reaction) is limited by surface reaction kinetics rather than Li^+ mass transport, thus the relationship between the peak current i_p and scan rate ν cannot be described by the Randles−Sevcik equation. Instead, the peak current is proportional to the scan rate following a capacitive-type mechanism as expressed by[28]

$$i_p = \frac{n^2F^2}{4RT}\nu A C_S^* \tag{2}$$

where n is the number of electrons transferred in the lithiation of sulfur (n = 2), F is the Faraday constant, R is the gas constant, T is the temperature (298.15 K), A is the specific surface area of the electrode with respect to the subnano confined sulfur (constant at 0.2 m^2 g^{-1} in all CV experiments), and C_s^* is the surface concentration of the lithiated sulfur. As the plot of the cathodic peak current i_p versus scan rate ν shows in Figure 6f, i_p displays an excellent linear relationship with ν in all electrolytes with different slopes. According to eq 2, the lithiated sulfur concentration in different electrolytes is calculated from the slope of i_p versus ν and listed in Table 3. The result of lithiated sulfur agrees very well with the trend of

DOI: 10.1021/acs.jpclett.8b00567
J. Phys. Chem. Lett. 2018, 9, 1739−1745

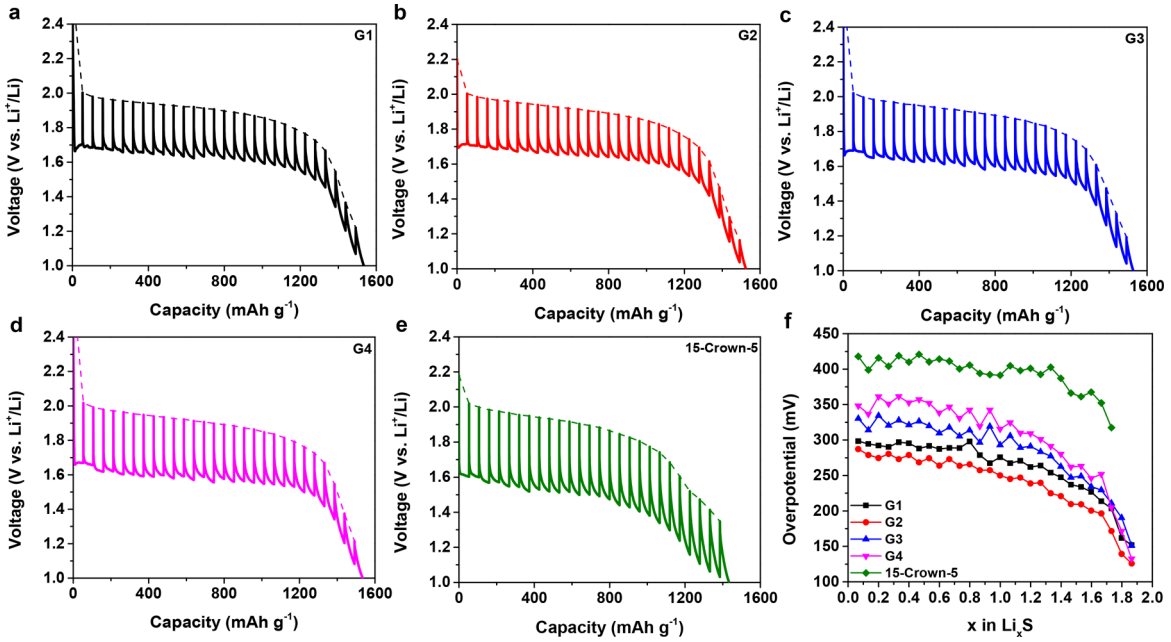

Figure 5. GITT curves of lithiation of subnano confined sulfur in (a) G1, (b) G2, (c) G3, (d) G4, and (e) 15-crown-5; (f) the overpotentials in all electrolytes from GITT.

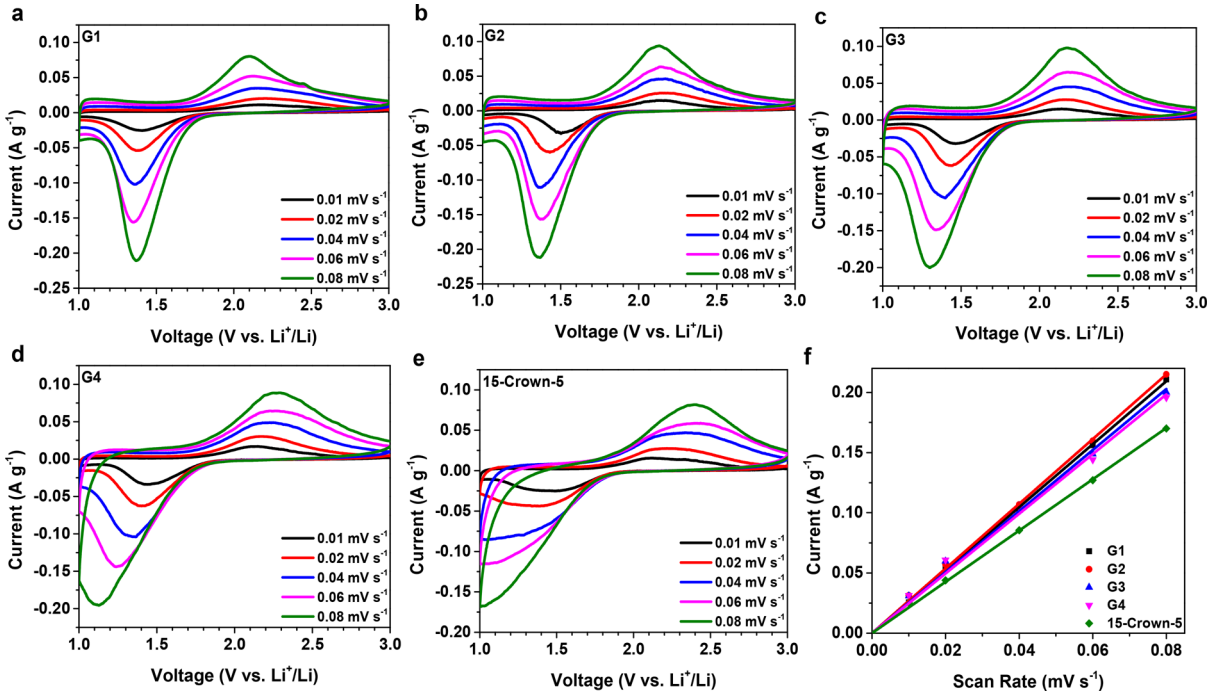

Figure 6. Slow scan CV of subnano confined sulfur versus Li^+/Li in (a) G1, (b) G2, (c) G3, (d) G4, and (e) 15-crown-5 electrolytes at various scan rates, and (f) cathodic peak current versus scan rate in the electrolytes.

Table 3. Lithiated Sulfur Concentration Obtained from Slow Scan CV in Different Electrolytes

	G1	G2	G3	G4	15-crown-5
$C_s^*(10^{-3}$ mol $m^{-2})$	3.46	3.53	3.36	3.28	2.82

overpotentials in these electrolytes as $C_{s\,(15\text{-crown-5})}^* < C_{s\,(G4)}^* < C_{s\,(G3)}^* < C_{s\,(G1)}^* < C_{s\,(G2)}^*$; consequently, a higher overpotential results in a lower concentration of lithiated sulfur.

In summary, we establish a firm correlation between the solvation structures of Li^+ in varying ether electrolytes and their kinetics in electrochemically lithiating sulfur in subnano confinement. AIMD simulations precisely predict a preferred 4-oxygen coordination shell for each Li^+ in ether solvents ranging from G1 to G4, with the exception of 15-crown-5, whose rigid ring structure dictates a 5-oxygen solvation shell. Interestingly, although the most stable Li^+ ion solvation structure in G2 is a 4-oxygen coordination shell involving two G2 molecules (one G2 contributes 3 Li−O linkages and the other G2 contributes one Li−O linkage), classical MD simulations show that a 3-coordinated solvation structure of

DOI: 10.1021/acs.jpclett.8b00567
J. Phys. Chem. Lett. 2018, 9, 1739−1745

$[Li(G2)]^+$ also exists due to the transient exchange of the G2 molecule, which only contributes one Li−O coordination. All predicted Li^+ solvation structures are confirmed with electrospray ionization-mass spectroscopy. Furthermore, the solvation binding energies in all the ether solvents are also calculated from AIMD simulations, and the results show an excellent correlation to the overpotentials of the lithiation of sulfur in subnano confinement. With further validation by GITT and slow scan CV results, we convincingly show that a higher solvation binding energy leads to a higher sulfur lithiation overpotential in the order of $\eta_{15\text{-crown-}5} > \eta_{G4} > \eta_{G3} > \eta_{G1} > \eta_{G2}$. The lowest overpotential in the G2 solvent can be attributed to the coexistence of a 3-coordinated $[Li(G2)]^+$ species, of which a lower activation energy barrier is required due to the partially desolvated Li^+. The mechanistic understanding achieved at an electronic and atomistic level of detail in this work provides us invaluable guidance regarding how one could manipulate the electrochemical kinetics of lithium−sulfur reactions in order to enhance sulfur cathode materials for electrochemical energy storage technologies.

■ ASSOCIATED CONTENT

Supporting Information

The Supporting Information is available free of charge on the ACS Publications website at DOI: 10.1021/acs.jpclett.8b00567.

Experimental details, discussion of negligible concentration overpotentials, computational methods, nitrogen adsorption−desorption isotherms and pore size distribution of the microporous carbon, TGA and XRD of subnano confined sulfur in microporous carbon host, representative AIMD simulation box, and structures of solvation complexes of $[Li(G2)]^+$ and $[Li(G2)_2]^+$ (PDF)

■ AUTHOR INFORMATION

Corresponding Authors

*E-mail: jguo@engr.ucr.edu; Web: http://www.cee.ucr.edu/jguo.

*E-mail: bryan.wong@ucr.edu; Web: http://www.bmwong-group.com.

ORCID

Mallory Gobet: 0000-0001-9735-0741

Kang Xu: 0000-0002-6946-8635

Bryan M. Wong: 0000-0002-3477-8043

Juchen Guo: 0000-0001-9829-1202

Author Contributions

⊥These authors contributed equally.

Notes

The authors declare no competing financial interest.

■ ACKNOWLEDGMENTS

J.G. and B.M.W. acknowledge the National Science Foundation for financial support under Grant No. CBET-1604908.

■ REFERENCES

(1) Choi, N. S.; Chen, Z. H.; Freunberger, S. A.; Ji, X. L.; Sun, Y. K.; Amine, K.; Yushin, G.; Nazar, L. F.; Cho, J.; Bruce, P. G. Challenges Facing Lithium Batteries and Electrical Double- Layer Capacitors. *Angew. Chem., Int. Ed.* **2012**, *51*, 9994−10024.

(2) Wang, D.; Zeng, Q.; Zhou, G.; Yin, L.; Li, F.; Cheng, H.; Gentle, I. R.; Lu, G. Q. Carbon/Sulfur Composites for Li-S Batteries: Status and Prospects. *J. Mater. Chem. A* **2013**, *1*, 9382−9394.

(3) Rosenman, A.; Markevich, E.; Salitra, G.; Aurbach, D.; Garsuch, A.; Chesneau, F. F. Review on Li-Sulfur Battery Systems: an Integral Perspective. *Adv. Energy Mater.* **2015**, *5*, 1500212.

(4) Manthiram, A.; Fu, Y.; Chung, S. H.; Zu, C. X.; Su, Y. S. Rechargeable Lithium Sulfur Batteries. *Chem. Rev.* **2014**, *114*, 11751−11787.

(5) Fu, C. Y.; Wong, B. M.; Bozhilov, K. N.; Guo, J. C. Solid State Lithiation-Delithiation of Sulphur in Sub-nano Confinement: A New Concept for Designing Lithium-Sulphur Batteries. *Chem. Sci.* **2016**, *7*, 1224−1232.

(6) Zhang, B.; Qin, X.; Li, G. R.; Gao, P. Enhancement of Long Stability of Sulfur Cathode by Encapsulating Sulfur into Micropores of Carbon Spheres. *Energy Environ. Sci.* **2010**, *3*, 1531−1537.

(7) Xin, S.; Gu, L.; Zhao, N.; Yin, Y.; Zhou, L.; Guo, Y.; Wan, L. Smaller Sulfur Molecules Promise Better Lithium-Sulfur Batteries. *J. Am. Chem. Soc.* **2012**, *134*, 18510−18513.

(8) Li, Z.; Jiang, Y.; Yuan, L.; Yi, Z.; Wu, C.; Liu, Y.; Strasser, P.; Huang, Y. A Highly Ordered Meso@Microporous Carbon-Supported Sulfur@Smaller Sulfur Core−Shell Structured Cathode for Li−S Batteries. *ACS Nano* **2014**, *8*, 9295−9303.

(9) Li, Z.; Yin, L. Nitrogen-Doped MOF-Derived Micropores Carbon as Immobilizer for Small Sulfur Molecules as a Cathode for Lithium Sulfur Batteries with Excellent Electrochemical Performance. *ACS Appl. Mater. Interfaces* **2015**, *7*, 4029−4038.

(10) Zhang, S. S. Sulfurized Carbon: A Class of Cathode Materials for High Performance Lithium/Sulfur Batteries. *Front. Energy Res.* **2013**, *1*, 1−9.

(11) Wang, D.-W.; Zhou, G. M.; Li, F.; Wu, K.-H.; Lu, G. M.; Cheng, H.-M.; Gentle, I. A Microporous-Mesoporous Carbon with Graphitic Structure for a High-Rate Stable Sulfur Cathode in Carbonate Solvent-Based Li-S Batteries. *Phys. Chem. Chem. Phys.* **2012**, *14*, 8703−8710.

(12) Li, Z.; Yuan, L.; Yi, Z.; Sun, Y.; Liu, Y.; Jiang, Y.; Shen, Y.; Xin, Y.; Zhang, Z.; Huang, Y. Insight into the Electrode Mechanism in Lithium-Sulfur Batteries with Ordered Microporous Carbon Confined Sulfur as the Cathode. *Adv. Energy Mater.* **2014**, *4*, 1301473.

(13) Markevich, E.; Salitra, G.; Rosenman, A.; Talyosef, Y.; Chesneau, F.; Aurbach, D. The Effect of a Solid Electrolyte Interphase on the Mechanism of Operation of Lithium-Sulfur Batteries. *J. Mater. Chem. A* **2015**, *3*, 19873−19883.

(14) Markevich, E.; Salitra, G.; Talyosef, Y.; Chesneau, F.; Aurbach, D. Review—On the Mechanism of Quasi-Solid-State Lithiation of Sulfur Encapsulated in Microporous Carbons: Is the Existence of Small Sulfur Molecules Necessary? *J. Electrochem. Soc.* **2017**, *164*, A6244−A6253.

(15) Han, S.; Yun, S.; Borodin, O.; Seo, D. M.; Sommer, R. D.; Young, V. G.; Henderson, W. A. Solvate Structures and Computational/Spectroscopic Characterization of $LiPF_6$ Electrolytes. *J. Phys. Chem. C* **2015**, *119*, 8492−8500.

(16) Blint, R. J. Binding of Ether and Carbonyl Oxygens to Lithium Ion. *J. Electrochem. Soc.* **1995**, *142*, 696−702.

(17) Henderson, W. A.; Brooks, N. R.; Brennessel, W. W.; Young, V. G. Triglyme−Li^+ Cation Solvate Structures: Models for Amorphous Concentrated Liquid and Polymer Electrolytes (I). *Chem. Mater.* **2003**, *15*, 4679−4684.

(18) Henderson, W. A.; Brooks, W. W.; Young, V. G. Tetraglyme−Li^+ Cation Solvate Structures: Models for Amorphous Concentrated Liquid and Polymer Electrolytes (II). *Chem. Mater.* **2003**, *15*, 4685−4690.

(19) Weast, R. C.; Astle, M. J. *CRC Handbook of Chemistry and Physics*, 62nd ed.; CRC Press: Boca Raton, FL, 1981.

(20) Carbone, L.; Gobet, M.; Peng, J.; Devany, M.; Scrosati, B.; Greenbaum, S.; Hassoun, J. Comparative Study of Ether-Based Electrolytes for Application in Lithium-Sulfur Battery. *ACS Appl. Mater. Interfaces* **2015**, *7*, 13859−13865.

(21) Ueno, K.; Tatara, R.; Tsuzuki, S.; Saito, S.; Doi, H.; Yoshida, K.; Mandai, T.; Matsugami, M.; Umebayashi, Y.; Dokko, K.; et al. Li^+ Solvation in Glyme−Li Salt Solvate Ionic Liquids. *Phys. Chem. Chem. Phys.* **2015**, *17*, 8248−8257.

DOI: 10.1021/acs.jpclett.8b00567
J. Phys. Chem. Lett. 2018, 9, 1739−1745

(22) Aguilera, L.; Xiong, S.; Scheers, J.; Matic, A. A Structural Study of LiTFSI−Tetraglyme Mixtures: from Diluted Solutions to Solvated Ionic Liquids. *J. Mol. Liq.* **2015**, *210*, 238−242.
(23) Saito, S.; Watanabe, H.; Ueno, K.; Mandai, T.; Seki, S.; Tsuzuki, S.; Kameda, Y.; Dokko, K.; Watanabe, M.; Umebayashi, Y. Li^+ Local Structure in Hydrofluoroether Diluted Li-glyme Solvate Ionic Liquid. *J. Phys. Chem. B* **2016**, *120*, 3378−3387.
(24) Boyer, M. J.; Vilciauskas, L.; Hwang, G. S. Structure and Li^+ Ion Transport in a Mixed Carbonate/$LiPF_6$ Electrolyte near Graphite Electrode Surfaces: A Molecular Dynamics Study. *Phys. Chem. Chem. Phys.* **2016**, *18*, 27868−27876.
(25) von Cresce, A.; Xu, K. Preferential Solvation of Li^+ Directs Formation of Interphase on Graphitic Anode. *Electrochem. Solid-State Lett.* **2011**, *14*, A154−A156.
(26) Callsen, M.; Sodeyama, K.; Futera, Z. k.; Tateyama, Y.; Hamada, I. The Solvation Structure of Lithium Ions in an Ether Based Electrolyte Solution from First-Principles Molecular Dynamics. *J. Phys. Chem. B* **2017**, *121*, 180−188.
(27) Fan, X.; Wu, H.; Shen, Z.; Kuo, J.-L. First-Principle Study on the Structure, Stability and Hardness of Cubic BC_2N. *Diamond Relat. Mater.* **2009**, *18*, 1278−1282.
(28) Bard, A. J.; Faulkner, L. R. *Electrochemical Methods: Fundamentals and Applications*; Wiley: New York, 2001; pp 591.

DOI: 10.1021/acs.jpclett.8b00567
J. Phys. Chem. Lett. 2018, 9, 1739−1745

Supporting Information

Correlating Li^+-Solvation Structure and its Electrochemical Reaction Kinetics with Sulfur in Sub-nano Confinement

Chengyin Fu[1‡], Lihua Xu[1‡], Fredy W. Aquino[2], Arthur v. Cresce[3], Mallory Gobet[4], Steven G. Greenbaum[4], Kang Xu[3], Bryan M. Wong[1,2], Juchen Guo[1,2]**

[1]Department of Chemical and Environmental Engineering, University of California, Riverside, CA 92521, United States.
[2]Materials Science and Engineering Program, University of California, Riverside, CA 92521, United States.
[3]U. S. Army Research Laboratory, Adelphi, MD 20783, United States.
[4] Department of Physics and Astronomy, Hunter College of the City University of New York, New York, NY 10065, United States.

Experimental Section

Preparation of Sub-nano Confined Sulfur: 300 mg sulfur (Sigma-Aldrich) was dissolved into carbon disulfide (CS_2, Sigma-Aldrich) which was mixed with 200 mg of microporous carbon with an average pore size of 0.67 nm (Kuraray Chemical Co., Japan). After drying at 60 °C overnight, the mixture was heated at 155 °C at a heating rate of 5 °C min^{-1} in a sealed stainless-steel vessel (with glass lining) filled with argon for 10 hours. The sub-nano confined sulfur was obtained by further heat-treating the composite at 200 °C in flowing argon for 6 hours to completely remove the sulfur deposited on the surface.

Materials Characterizations: The nitrogen adsorption-desorption isotherm of the microporous carbon was obtained with a surface area analyzer (Micromeritics ASAP2020). The nitrogen adsorption-desorption isotherms and pore size distribution of the microporous carbon are shown in **Figure S1**. Thermogravimetric analysis (TGA, TA Instruments Q500) was used to measure the sulfur content in the composites (**Figure S2**). The crystal structure of the sulfur in the composites was characterized with X-ray powder diffraction (XRD, PANalytical Empyrean) (**Figure S3**).

Electrochemical Measurements: The electrodes were comprised of 70 wt.% sulfur-carbon composite, 20 wt.% carbon black (Super P), and 10 wt.% poly(vinylidene fluoride) (Sigma-Aldrich) binder. The sulfur areal loading was consistently at 0.5 mg cm^{-2} in all electrodes. Aluminum foil (99.45%, Alfa Aesar) was used as the current collector. Three-electrode cylindrical cells (MTI) with lithium foil (Alfa Aesar) as the counter electrode and reference electrode were assembled in an argon-filled glovebox for the electrochemistry analysis. Electrolytes consisting of 0.5 M LiTFSI (Sigma-Aldrich) in G1, G2, G3, G4, and 15-crown-5 (Sigma-Aldrich) were used with a microporous membrane separator (Celgard 2500). Slow scan CV measurements were carried out with

different scan rates using a Gamry Interface 1000 analyzer. For GITT experiments, the electrodes were lithiated at 50 mA g^{-1} for 1 hour and then allowed to rest for 16 hours. The lithiation-rest process was repeated until the potential reached 1 V vs. Li^+/Li. All the electrochemical measurements were performed at room temperature. The IR drop was removed from the GITT curves.

Discussion of Concentration Overpotential in the GITT Experiments:

The concentration overpotential is induced by the concentration gradients in the diffusion layer adjunct to the electrode, and it can be expressed as[1]

$$\eta_c = \frac{RT}{nF} \ln\left(1 - \frac{i}{i_L}\right),$$

where R is the gas constant, T is the temperature (23 ºC), n is the number of electrons transferred in the sulfur lithiation (n = 2), F is the Faraday constant, i is the current density, and i_L is the diffusion limiting current density, which can be written as[1]

$$i_L = \frac{DnFC_B}{\delta},$$

where D is the self-diffusion coefficient of solvated Li^+ (listed in Table 1), C_B is the bulk concentration of Li^+ ions in the electrolyte (0.5 M), and δ is the thickness of the diffusion layer. The lowest self-diffusion coefficient of the solvated Li^+ ions is 0.147×10^{-10} m^2 s^{-1}. The diffusion layer thickness δ in our three-electrode cells can be expected to be much smaller than the thickness of the separator, which is 2.5×10^{-5} m. Therefore, the diffusion limiting current density i_L can be estimated to be higher than 5.67 mA cm^{-2}. The current density applied in the GITT current pulse is i = 0.025 mA cm^{-2}. Therefore, the maximum concentration overpotential η_c can be estimated as ~0.056 mV. As a result, it is negligible in our GITT experiments, and the overpotential in the lithiation of sub-nano confined sulfur is only attributed to the activation overpotential.

Computational Methodologies: The various ether solvent molecules (e.g. G1 to 15-crown-5) and the anion $[TFSI]^-$ were optimized using the NWChem[2] quantum chemistry software with the def2-TZVP[3] basis set and B3LYP hybrid functional[4, 5]. Based on a 0.5 M LiTFSI concentration, the initial box structures contain 1 Li^+ ion, 1 TFSI anion, and a stoichiometric number of GX molecules: 19 G1, 14 G2, 11 G3, 9 G4, and 10 G5, respectively. The initial box for G1 is shown in **Figure S4** as a representative. These simulation structures were generated using the AMBER[6] and PACKMOL[7] codes. We minimize the energy using SANDER followed by two classical MD simulations that use general AMBER force-field parameters[8]. The first simulation uses the NVT ensemble for 1 ns (1 fs time step) at a high temperature of T = 1200 K for overcoming potential energy barriers to enhance conformational samplings.[9, 10] The second simulation uses the NPT ensemble for 2 ns (1 fs time step) at P = 1 bar and T = 298 K. The production part for analyzing our results in the classical MD calculations comprise the last 1 ns of the second simulation. Structures are then selected from the trajectory (in the production part) for the subsequent *Ab-Initio* MD (AIMD) simulations.

The AIMD simulations compute quantum-mechanically derived forces using VASP-DFT[11-13], and we adopted the PBE[14] exchange-correlation functional together with the D3-BJ[15] damping correction, which we found in a previous study to accurately account for dispersion interactions.[16-17] It is worth noting that VASP uses projector augmented wave (PAW) pseudopotentials in a plane wave implementation which gives results at a quality of an all-electron calculation. The VASP calculations used a 500 eV energy cutoff for the plane wave expansion of the wave functions and the Brillouin zone was sampled only at the Γ-point (due to the large unit cell). The simulation was performed with an NVT ensemble at room temperature (298 K) with a Nosé thermostat.[18, 19] The final production part for our subsequent analysis comprise the last 10 ps from the AIMD simulations with a time step of 1 fs after the previous 5 ps equilibration procedure.

To shed additional insight into the binding energies of $[Li(G2)_2]^+$ and $[Li(G2)]^+$ (depicted in **Figure S5**), we carried out additional geometry optimizations using the all-electron Gaussian code. We utilized the same convention (from the VASP calculations) for the binding energy defined as

$$E_b = (E_t - E_{TFSI} - nE_{G2} - E_{Li})$$

where E_b is the binding energy per Li^+ ion; E_t is the total energy of the solvation complex, which is -2758.37649973 Hartrees for $[Li(G2)_2]^+$ and -2296.09348699 Hartrees for $[Li(G2)]^+$; E_{TFSI} is the energy of the TFSI anion, which is -1826.08437124 Hartrees; n is the number of G2 molecules (n = 2 in $[Li(G2)_2]^+$ and n = 1 in $[Li(G2)]^+$) in the complex; E_{G2} is the energy of G2, which is -462.251638574 Hartrees; and E_{Li} is the energy of Li^+ cation, which is -7.46001570675 Hartrees. With these energies, we obtained $E_b([Li(G2)_2]^+)$ = -0.328835635 Hartree = -8.94807801 eV and $E_b([Li(G2)]^+)$ = -0.297460794 Hartrees = -8.09432465 eV. Although these binding energies cannot be directly compared to the ones obtained from AIMD simulations (the AIMD simulations use plane-wave pseudopotentials whereas the Gaussian calculations use all-electron localized basis sets), the trend validates that the binding energy of $[Li(G2)_2]^+$ is stronger than $[Li(G2)]^+$.

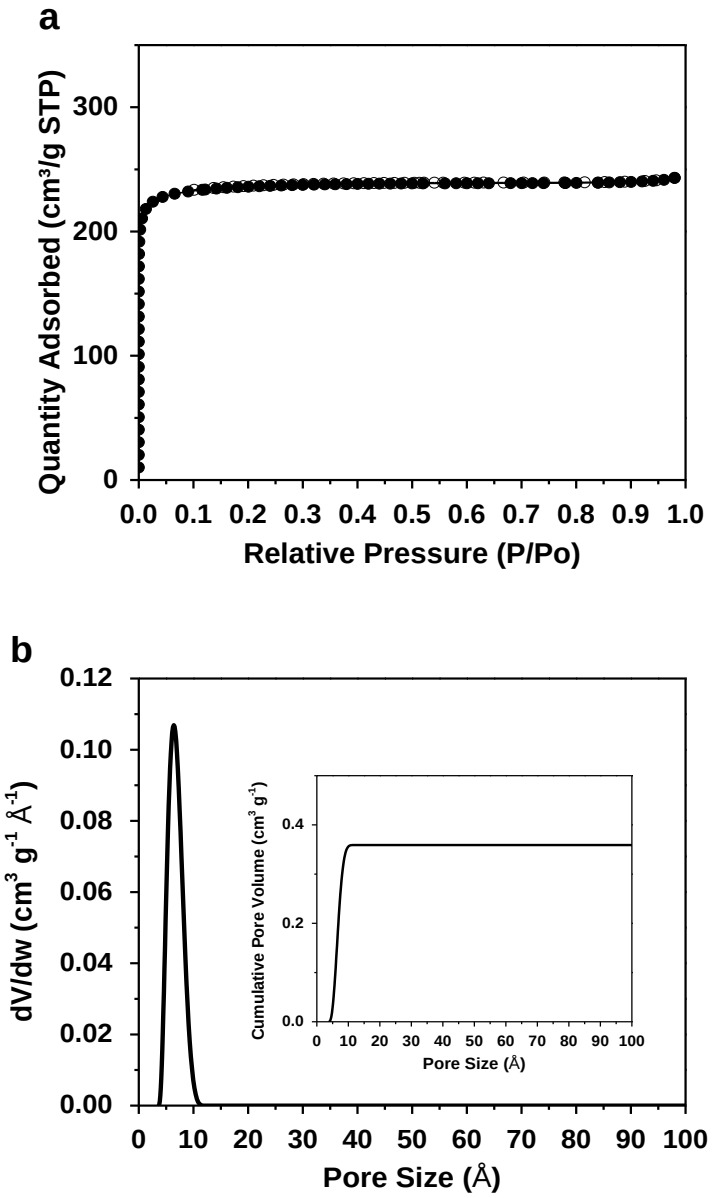

Figure S1. (a) Nitrogen adsorption–desorption isotherm and (b) pore size distributions (cumulative pore volume as inset) of the microporous carbon. Fig. S1a shows the type-I nitrogen adsorption–desorption isotherms of the microporous carbon, and Fig. S1b shows its pore size distributions calculated based on a non-local density functional theory (NLDFT) model.

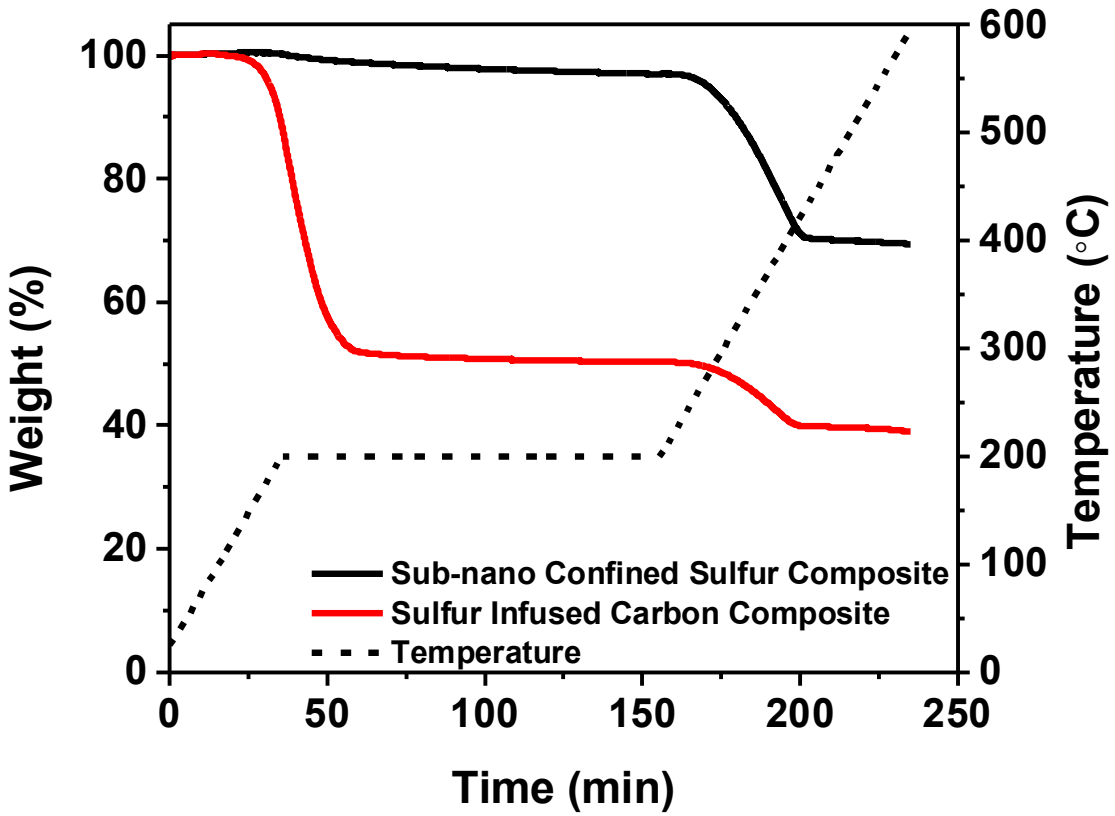

Figure S2. TGA curves of the sulfur-carbon composite with sub-nano confined sulfur. Thermogravimetric analysis (TGA) was performed in argon from room temperature to 600 °C with a heating ramp of 5 °C min^{-1}, and a 2-hour isothermal step was imposed at 200 °C. As shown by the red curve, the TGA result shows that the composite contains 60 wt.% of sulfur after sulfur infusion and has two weight loss stages. The first weight loss stage is at the isothermal step at 200 °C, and it is due to the sublimation of the sulfur deposited on the surface of the carbon host. The second weight loss starts at 270 °C and completes at 400 °C, and arises from the sublimation of the sulfur confined in the sub-nano pores of the carbon host. Since we intended to investigate the sub-nano confined sulfur, superficial sulfur was removed at 200 °C in flowing argon for 6 hours to obtain only sub-nano confined sulfur. As shown by the black curve, after superficial sulfur removal, the TGA curve only shows the second weight loss stage, which indicates that the sulfur is only encapsulated in sub-nano pores.

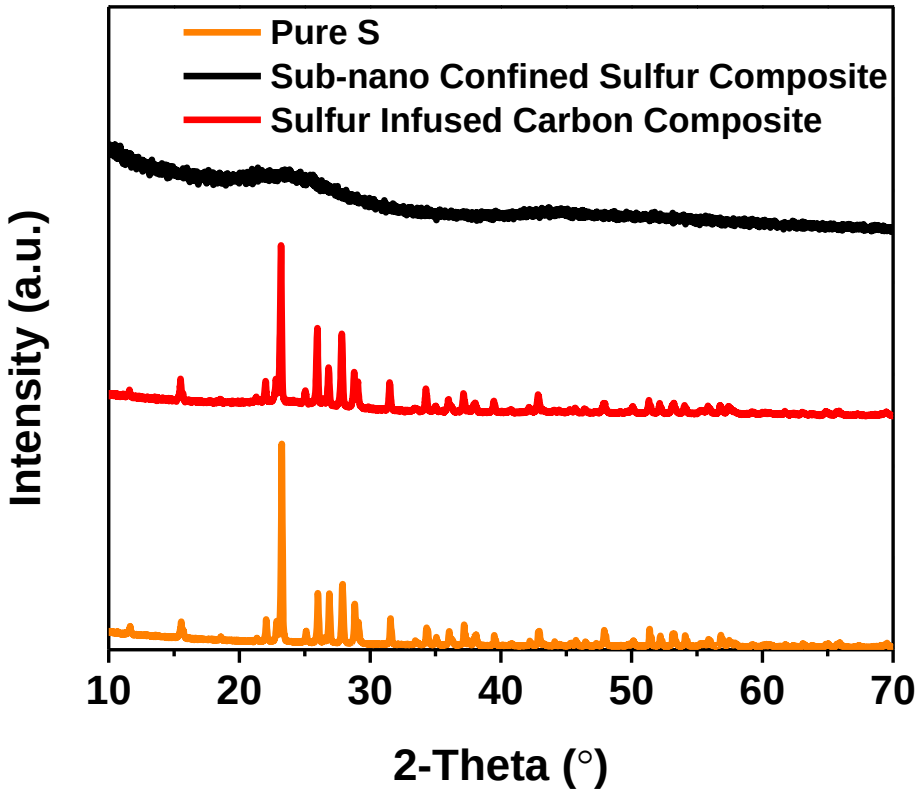

Figure S3. XRD patterns of elemental sulfur, sulfur infused microporous carbon composite (red), and the composite with sub-nano confined sulfur (black). Before superficial sulfur removal, the carbon-sulfur composite shows a crystalline sulfur pattern, which indicates the existence of bulk sulfur outside the sub-nano pores. The XRD pattern of the microporous carbon with sub-nano confined sulfur is amorphous, which suggests a complete removal of bulk sulfur.

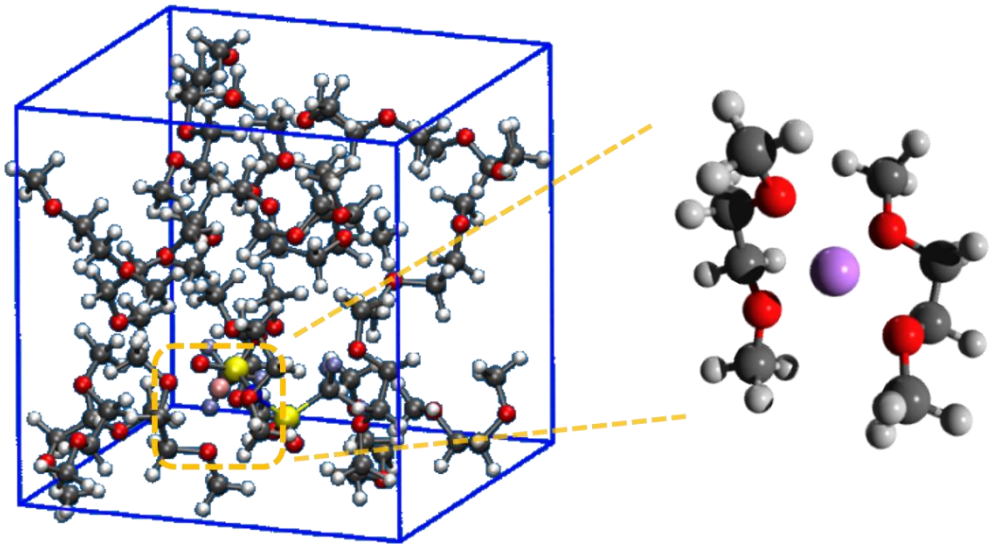

Figure S4. Simulation box showing the structure for Li[TFSI]/G1 (left) and a magnified view of a representative solvation structure of the Li^+ ion (right). Color code: purple: Li, blue: N, yellow: S, red: O, grey: C, cyan: F, and white: H.

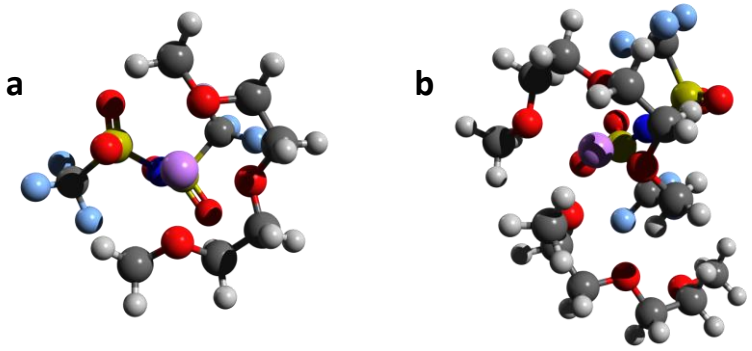

Figure S5. Structure of solvation complex of (a) $[Li(G2)]^+$ and (b) $[Li(G2)_2]^+$. Color code: purple: Li, blue: N, yellow: S, red: O, grey: C, cyan: F, and white: H.

REFERENCES

(1) Bard, A. J.; Faulkner, L. R. Electrochemical Methods: Fundamentals and Applications; Wiley: New York, 2001; pp 29-33.

(2) Bylaska, E.; et al.; De Jong, W.; Govind, N.; Kowalski, K.; Straatsma, T.; Valiev, M.; Wang, D.; Apra, E.; Windus, T.; Hammond, J. NWChem, A Computational Chemistry Package for Parallel Computers, version 5.1. *Pacific Northwest National Laboratory, Richland, Washington* **2007,** *99352*, 0999.

(3) Weigend, F.; Ahlrichs, R. Balanced Basis Sets of Split Valence, Triple Zeta Valence and Quadruple Zeta Valence Quality for H to Rn: Design and Assessment of Accuracy. *Phys. Chem. Chem. Phys.* **2005,** *7*, 3297-3305.

(4) Becke, A. D. A New Mixing of Hartree–Fock and Local Density-Functional Theories. *J. Chem. Phys.* **1993,** *98*, 1372-1377.

(5) Stephens, P.; Devlin, F.; Chabalowski, C.; Frisch, M. J. Ab Initio Calculation of Vibrational Absorption and Circular Dichroism Spectra using Density Functional Force Fields. *J. Phys. Chem.* **1994,** *98*, 11623-11627.

(6) Case, D. A.; Betz, R. M.; Cerutti, D. S.; Cheatham, T. E., III; Darden, T. A.; Duke, R. E.; Giese, T. J.; Gohlke, H.; Goetz, A. W.; Homeyer, N.; *et al.* AMBER 2016; University of California: San Francisco, CA, 2016.

(7) Martínez, L.; Andrade, R.; Birgin, E. G.; Martínez, J. M. PACKMOL: A Package for Building Initial Configurations for Molecular Dynamics Simulations. *J. Comput. Chem.* **2009,** *30*, 2157-2164.

(8) Wang, J.; Wolf, R. M.; Caldwell, J. W.; Kollman, P. A.; Case, D. A. Development and Testing of a General Amber Force Field. *J. Comput. Chem.* **2004,** *25*, 1157-1174.

(9) Kannan, S.; Zacharias, M. Folding of Trp-cage Mini Protein Using Temperature and Biasing Potential Replica—Exchange Molecular Dynamics Simulations. *Int. J. Mol. Sci.* **2009,** *10*, 1121-1137.

(10) Leach, A. R. 4.05 - Ligand-Based Approaches: Core Molecular Modeling A2 - Taylor, John B. In *Comprehensive Medicinal Chemistry II*, Triggle, D. J., Ed. Elsevier: Oxford, 2007; pp 87-118.

(11) Kresse, G.; Furthmüller, J. Efficient Iterative Schemes for Ab Initio Total-Energy Calculations using a Plane-Wave Basis Set. *Phys. Rev. B* **1996,** *54*, 11169.

(12) Kresse, G.; Hafner, J. Ab Initio Molecular Dynamics for Liquid Metals. *Phys. Rev. B* **1993,** *47*, 558.

(13) Kresse, G.; Joubert, D. From Ultrasoft Pseudopotentials to the Projector Augmented-Wave Method. *Phys. Rev. B* **1999,** *59*, 1758.

(14) Perdew, J. P.; Burke, K.; Ernzerhof, M. Generalized Gradient Approximation Made Simple. *Phys. Rev. Lett.* **1996,** *77*, 3865.

(15) Grimme, S.; Ehrlich, S.; Goerigk, L. Effect of the Damping Function in Dispersion Corrected Density Functional Theory. *J. Comput. Chem.* **2011,** *32*, 1456-1465.

(16) Ilawe, N. V.; Zimmerman, J. A.; Wong, B. M. Breaking Badly: DFT-D2 Gives Sizeable Errors for Tensile Strengths in Palladium-Hydride Solids. *J. Chem. Theory Comput.* **2015**, *11*, 5426-5435.

(17) Anderson, L. N.; Aquino, F. W.; Raeber, A. E.; Chen, X.; Wong, B. M. Halogen Bonding Interactions: Revised Benchmarks and a New Assessment of Exchange vs Dispersion. *J. Chem. Theory Comput.* **2018**, *14*, 180-190.

(18) Hoover, W. G. Canonical Dynamics: Equilibrium Phase-Space Distributions. *Phys. Rev. A* **1985,** *31*, 1695-1697.

(19) Nosé, S. A Unified Formulation of the Constant Temperature Molecular Dynamics Methods. *J. Chem. Phys.* **1984,** *81*, 511-519.